Journal of
Experimental and Theoretical Analyses

MDPI

Article

The Performance of Large Diameter Threaded Cast Iron Pipe Fitting Joints Used in a Fire Suppression System: Experimental and Fragility Analysis

Cameron Rusnak [1,*], Sherif Elfass [2] and Allen Rivas [2]

[1] Institute of Technology, School of Engineering, West Virginia University, Beckley, WV 25801, USA
[2] Department of Civil and Environmental Engineering, University of Nevada, Reno, NV 89557, USA; elfass@unr.edu (S.E.); allenjohnrivas@gmail.com (A.R.)
* Correspondence: cameron.rusnak@mail.wvu.edu

Abstract

Threaded cast iron fittings, including tees and elbows, are commonly used in fire suppression systems to connect piping components due to their simplicity, reliability, and compatibility with National Pipe Thread (NPT) standards. While extensively used in practice, their structural performance under seismic demands, particularly for large-diameter fittings, remains insufficiently understood. Previous studies have primarily focused on smaller-diameter fittings or have idealized the fitting body as rigid, overlooking the potential for internal deformation and rupture. This study addresses this knowledge gap through an experimental investigation of 3-inch and 4-inch gray cast iron threaded elbow and tee fittings subjected to loading. A total of 18 full-scale assemblies were tested across multiple configurations. Results showed that structural rupture of the fitting body was the dominant failure mode, with no specimens reaching the defined threshold for substantial leakage. Limited early-stage leakage was observed in select 3-inch tee configurations prior to rupture. Damage State 3 (DS3), defined as rupture, occurred at rotational capacities ranging from 0.0061 to 0.0179 radians. Fitting stiffness to failure averaged approximately 643 kip-ft/rad. Fragility models were developed within a probabilistic framework, incorporating variability due to material imperfections and assembly tolerances. The findings reveal a size-dependent shift in behavior: 3-inch fittings demonstrated greater pipe rotation prior to failure, while 4-inch fittings exhibited higher internal stiffness but reduced flexibility. These results provide moment–rotation relationships and fragility models to support analytical modeling and seismic vulnerability assessments, advancing the predictive understanding of large-diameter threaded cast iron fittings used in fire suppression systems.

Keywords: pipe fittings; fragility analysis; rotational capacity; threaded connections; seismic performance; structural failure

Academic Editor: Marco Rossi

Received: 14 April 2026
Revised: 30 April 2026
Accepted: 7 May 2026
Published: 20 May 2026

1. Introduction

The operational performance of a building depends not only on its structural frame but also on its non-structural components, which include electrical, architectural, and mechanical systems. Historical evidence from past seismic events underscores the significant consequences of failures in these non-structural systems. In many cases, damage to non-structural elements has exceeded that of structural components, particularly in critical facilities such as hospitals, power plants, laboratories, and government buildings [1–3]. Among these, the fire suppression piping system represents a vital mechanical subsystem.

Its structural integrity is essential, not only for maintaining building functionality during and after a seismic event, but also for ensuring life safety by suppressing fires and limiting associated damage and loss.

Historical earthquakes have repeatedly demonstrated the vulnerability of non-structural systems to seismic events. For instance, the 1994 Northridge earthquake caused widespread disruption, including the collapse of ceiling tiles, shattering of glazing systems, and failure of HVAC and piping infrastructure, ultimately resulting in the temporary shutdown of numerous businesses [4–7]. In the 2011 Tohoku earthquake in Japan, non-structural damage, particularly to piping systems, was especially severe, contributing to approximately 49% of the total economic losses incurred [8]. Similarly, significant non-structural damage was observed during the 2010–2011 Canterbury earthquakes in New Zealand and the 2014 South Napa earthquake in California, further emphasizing the systemic vulnerability of mechanical and architectural components during seismic events [9,10]. Reconnaissance findings from the 2018 Palu earthquake, as reported by the University of Notre Dame, documented similar patterns of damage. The associated report includes Figure 1, which depicts the extent of non-structural failures observed at affected sites [11].

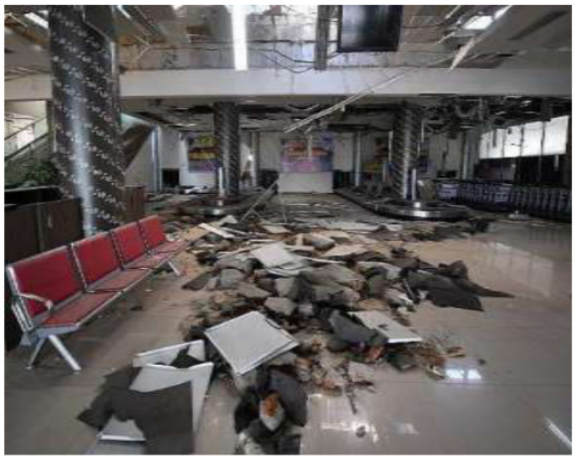

Figure 1. Non-Structural Damage that Occurred in the 2018 Palu Earthquake.

Extensive research has been conducted on the behavior of piping systems and their associated fittings, particularly in the context of seismic performance. Wang et al. [12] investigated the behavior of grooved fittings, presenting moment–rotation responses, observed damage states, and fragility characteristics based on experimental testing. Tian et al. [13] expanded the focus to pressurized fire suppression piping systems, examining both threaded and grooved fittings to evaluate their seismic capacity. The study provided valuable data on rotational behavior and system fragility. Zaghi et al. [14] examined seismic loading effects on hospital piping assemblies, with particular attention to drift ratio thresholds and their relationship to leakage potential. Qu et al. [15] explored the performance of PPR and galvanized steel pipes, generating fragility curves to characterize their seismic response across varying conditions. Antaki conducted two experimental studies on fire suppression piping assemblies. The first combined static and shake table tests to evaluate global system response, while the second utilized four-point bending to assess localized joint behavior [16,17]. Soroushian et al. [18,19] conducted rotational capacity testing on 48 grooved joints, providing detailed insight into their mechanical performance. Rusnak et al. [20] experimentally evaluated 1-, 1.5-, and 2-inch diameter elbow and tee fittings to assess their seismic resilience, developing corresponding rotational capacity measures and fragility models. Their study also highlighted the differing performance between threaded

and welded connections, emphasizing the need to distinguish between the two due to their distinct geometric configurations and mechanical properties [21]. Yoshizaki et al. [22] investigated the seismic performance of buried low-angle elbow pipelines subjected to permanent ground deformation, developing a method to estimate post-deformation angle changes supported by finite element (FE) modeling.

Larger structural components typically exhibit greater resistance to deformation and, as a result, demonstrate increased strength under applied loads [23]. The influence of size on mechanical properties has been studied across various material systems. Hou et al. [24] investigated the deformation behavior of pure copper wires, with particular attention to the role of free surface grains. Their findings indicated a clear trend: as wire diameter decreased, tensile strength was reduced, highlighting a size-dependent weakening mechanism. In the context of reinforced concrete structures, Chen et al. [25] examined the shear size effect in simply supported RC deep beams, offering insights into how cross-sectional dimensions influence shear strength and failure modes. Bai et al. [26] addressed size effects from a fatigue perspective by proposing a predictive model for the fatigue strength of large-scale components. Their work introduced a systematic approach for quantifying size effects through direct measurement, leading to the development of a reliable Load Effect Transformation (LET) model.

In the United States, fire suppression systems have traditionally relied on threaded joints to connect pipes to fittings, utilizing standardized National Pipe Thread (NPT) profiles to achieve sealed mechanical connections through torsional engagement [27]. NPT threads are manufactured in a wide range of nominal pipe sizes, from as small as 1/8 inch to as large as 24 inches in diameter; however, larger sizes are rarely employed in typical fire protection applications [28]. While the National Fire Protection Association (NFPA) does not explicitly define "large-diameter" fittings, components with nominal diameters of 3 inches and above are commonly treated as such in practice, largely due to their deviation from the more conventional 2½-inch connections used in standard system layouts and design criteria [29].

Although NFPA codes [30] and prior research have established comprehensive guidelines for the design and operational function of fire suppression systems, a critical knowledge gap remains regarding the seismic resilience and mechanical behavior of threaded cast iron pipe fittings, particularly those classified as large diameter. Much of the existing literature has focused on the rotational response and failure mechanisms at the pipe-thread interface, often modeling the fitting itself as a rigid body. This assumption overlooks the potential for deformation and rotational compliance within the fitting, which can significantly influence the global system response under seismic loading. For example, Qu et al. [15] reported fracture failures within the fitting body while using rotation at the pipe-fitting interface as the primary damage metric, suggesting that internal bending stresses within the fitting may have contributed to the observed damage. Similarly, methodologies employed by Yoshizaki et al. [22], Chapman Electric Supply [31], and WSSC [32] often idealize the joint as rigid, potentially underestimating the influence of fitting flexibility on system performance. These simplifications underscore the need for targeted investigations into the mechanical behavior of large-diameter threaded fittings and their adjoining pipe segments under representative loading conditions.

This study examines the rotational capacity, failure mechanisms, and seismic fragility of large-diameter threaded cast iron pipe fittings, specifically elbow and tee configurations in 3- and 4-inch nominal sizes. A total of 18 quasi-static tests were conducted to characterize the mechanical response of these components, identify critical damage states, and develop fragility curves tailored to each size and configuration. Building on prior investigations of smaller-diameter fittings (1–2 inches [20]), this study extends the experimental framework

to larger diameters to evaluate the influence of size on mechanical behavior and failure characteristics. In contrast to previous studies that primarily focused on smaller fittings and often emphasized leakage-based damage mechanisms, this work focuses on larger-diameter configurations and explicitly evaluates the role of fitting deformation and structural rupture in governing system response. In doing so, the work addresses a gap in understanding how threaded cast iron fittings respond under seismic demands as system scale increases. The results provide moment–rotation relationships and probabilistic fragility models for large-diameter fittings, offering input for analytical modeling and performance-based seismic assessment of fire suppression piping systems.

2. Materials and Methods

2.1. Threaded Cast Iron Pipe Fittings System

This study investigated large-diameter gray cast iron threaded fittings, with an emphasis on elbow and tee fittings, as depicted in Figure 2. The elbow fitting (Figure 2a), which forms a 90-degree bend, is designed to redirect flow at a right angle within the piping system. In contrast, the tee fitting (Figure 2b) consists of two orthogonal branches intersecting at a central point. This geometry enables the system to both continue along its original axis and simultaneously divert flow perpendicularly, such as when transitioning from branch lines into a main header.

(**a**) (**b**)

Figure 2. Threaded Cast Iron Fittings Tested: (**a**) Typical Large Threaded Cast Iron Elbow Fitting; (**b**) Typical Large Threaded Cast Iron Tee Fitting.

All cast iron components were manufactured in accordance with ASME standards, including prescribed thread tolerances and dimensional requirements [33–37]. The fittings used in this study were gray cast iron threaded fittings conforming to ASME B16.4 specifications, which are commonly produced in standard pressure classes (e.g., Class 125 or Class 250) for fire protection applications. The adjoining pipes consisted of carbon steel piping (Schedule 40), consistent with typical fire suppression system construction. These material selections were chosen to reflect representative field-installed systems.

The full system configuration consisted of steel pipes joined through a network of threaded fittings, valves, and couplers to replicate realistic operational conditions.

2.2. Experimental Setup and Loading Protocol

A total of eighteen (18) large-diameter pipe fitting assemblies were subjected to experimental testing, representing two nominal size categories: 3-inch and 4-inch diameters. In the context of this study, “large-diameter” threaded fittings are defined as nominal pipe sizes of 3 inches and greater. While National Fire Protection Association standards do not explicitly define this threshold, guidance from NFPA 13 [30] and supporting industry references indicate that fittings of 3 inches and above are commonly treated separately from standard 2½-inch system components due to differences in application and mechanical behavior. Three configurations were examined: (1) an elbow-pipe assembly, (2) a tee-pipe assembly in the primary loading configuration, where load was applied through the central

header pipe, and (3) a tee-pipe assembly in the secondary loading configuration, where load was applied through one of the distribution pipes. To ensure result reliability and capture variability, each configuration was tested in triplicate. The experimental setups are depicted in Figure 3: Figure 3a,b show the elbow configuration, Figure 3c,d show the tee configuration under primary loading, and Figure 3e,f show the tee configuration under secondary loading. In the figures, Pipe 1 and Pipe 3 (when present) denote the distribution lines, while Pipe 2 identifies the central header pipe.

Assembly of each test configuration was carried out by certified journeyman plumbers from Deer Plumbing LLC (License #0069124), using field-representative techniques consistent with the "skill of craft" standard commonly practiced in the plumbing industry. This approach was selected to replicate realistic installation conditions typical of actual system assemblies. Each test configuration was mounted to a 22-kip servo-hydraulic actuator via a hinged connection designed to release end moments at the point of load application. This setup permitted free in-plane rotation, allowing the assembly to deflect naturally in the loading direction.

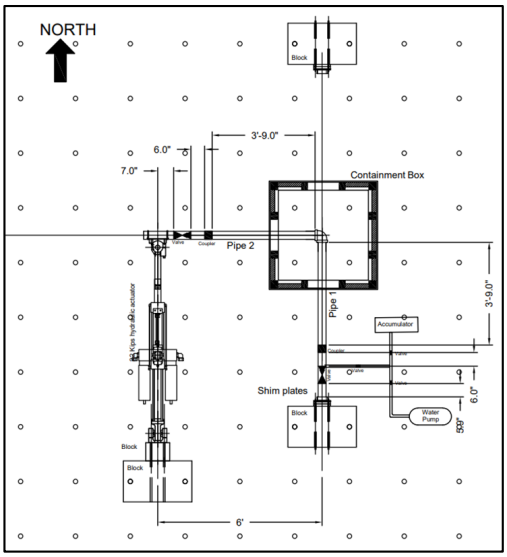

(**a**)

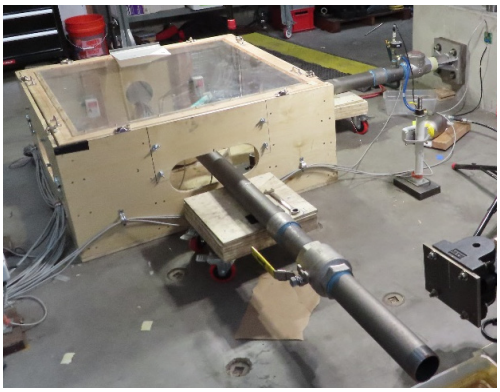

(**b**)

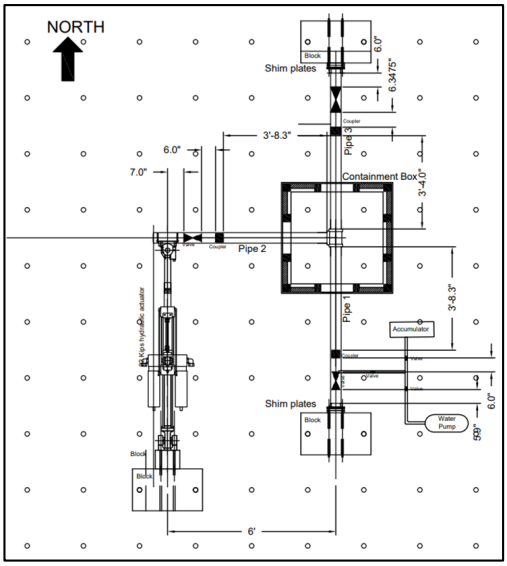

(**c**)

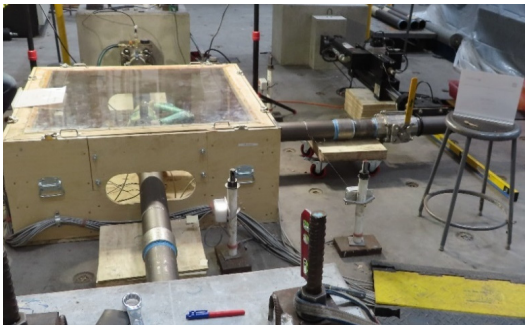

(**d**)

Figure 3. *Cont.*

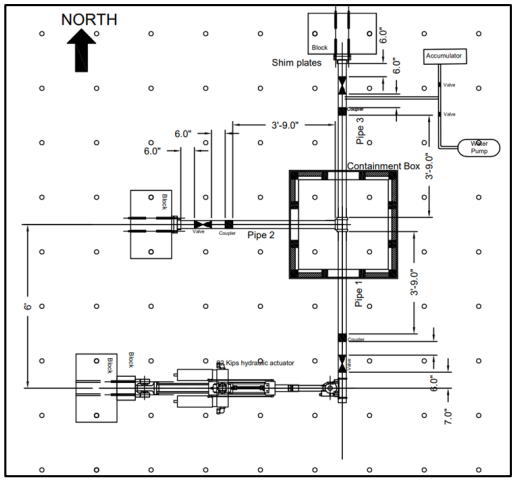

(**e**)

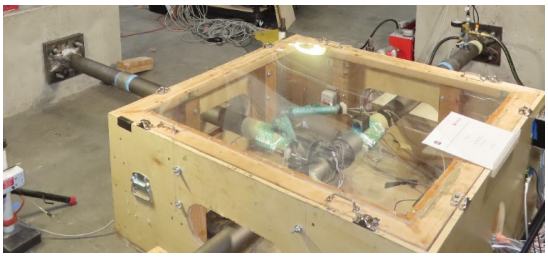

(**f**)

Figure 3. Laboratory Photos: (**a**) Elbow-Pipe Assembly Test Setup; (**b**) Elbow-Pipe Assembly Laboratory Photo; (**c**) Tee-Pipe Assembly in Primary Configuration Test Setup; (**d**) Tee-Pipe Assembly in Primary Configuration Laboratory Photo; (**e**) Tee-Pipe Assembly in Secondary Configuration Test Setup; (**f**) Tee-Pipe Assembly in Secondary Configuration Laboratory Photo.

To provide structural restraint and maintain system stability, the opposite end(s) of the assembly was anchored to reinforced concrete reaction blocks, which were fixed to the laboratory floor. The baseplates were connected using slip-critical bolts to prevent slippage during testing, and shimming plates were incorporated at the reaction block ends to enable fine positional adjustments. To ensure consistency and eliminate carryover effects, a new set of pipes and fittings was used for each test iteration. For safety, a containment enclosure surrounded the assembly to mitigate the risk of projectiles, debris, or fluid splash in the event of component failure.

The pipe lengths used on either side of the fittings were selected to isolate the fittings from boundary influences introduced by the actuator and reaction supports. These lengths were determined based on ensuring that flexural and displacement development within the pipe occurred without reflection of forces or constraints back onto the fittings. Although Federal Emergency Management Agency 461 [38] does not prescribe explicit minimum pipe lengths, it emphasizes the importance of realistic boundary conditions and the minimization of artificial constraints. Consistent with this guidance and prior experimental studies on piping systems, pipe lengths on the order of 8–12 times the pipe diameter have been shown to sufficiently reduce boundary effects. In this study, a minimum pipe length of ten times the pipe diameter ($\geq$10 D) was adopted as a conservative and widely accepted threshold to ensure that the measured response reflects the behavior of the fitting rather than boundary-induced artifacts.

Following construction, each assembly underwent a hydrostatic pressure test (HPT) prior to the application of any loading. This initial step served to validate system integrity by confirming the absence of any leaks. The HPT was conducted at an internal pressure of 200 $\pm$ 5 psi and was maintained continuously for a duration of two hours. Upon successful completion of the HPT, the internal pressure was reduced and stabilized at the nominal operational test pressure of 140 $\pm$ 5 psi in preparation for subsequent loading protocols.

The quasi-static loading protocol was developed in accordance with Interim Protocol I, as outlined in FEMA 461 [38], which provides a standardized methodology for assessing the seismic performance of structural and nonstructural components. This protocol facilitates the quantification of seismic demand, the identification of damage states, and the generation of fragility functions based on empirical data. The applied loading sequence in this study

adhered closely to the FEMA-specified guidelines, consisting of seventeen (17) discrete steps. Each step involved either a single displacement amplitude or two complete loading cycles. Displacement amplitudes increased in 0.5-inch increments, except for the initial step, with the loading sequence culminating in a maximum imposed displacement of 8 inches. The actuator displacement rate was maintained at 2.5 inches per minute up to 3.5 inches of displacement, after which the rate increased to 5 inches per minute. A graphical representation of the loading protocol is provided in Figure 4, and the full sequence of displacement cycles is detailed in Table 1.

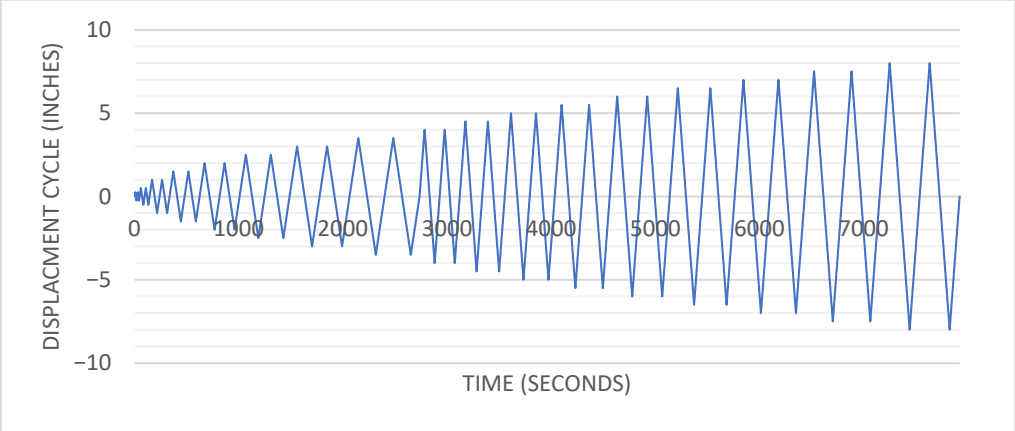

Figure 4. Visual Representation of the Loading Protocol Used.

Table 1. Description of Loading Protocol with Each Displacement Cycle Amplitude.

Deformation Amplitude (inch)	Loading Rate (inch/min)
0.25	2.5
0.5	
1	
1.5	
2	
2.5	
3	
3.5	
4	5
4.5	
5	
5.5	
6	
6.5	
7	
7.5	
8	

Test termination criteria were defined prior to the application of loading and were as follows:

1. Successful completion of the loading protocol without any observed failures.
2. Substantial water leakage at the pipe-fitting interface, equivalent to a volume of 2 ounces of water collected during the test.
3. Structural failure, including:
    a. Rupture of the fitting
    b. Rupture of the pipe

Criterion 1 does not represent the actual capacity of the fitting, but rather signifies the termination of testing. In contrast, Criteria 2 and 3 correspond to defined failure modes and are therefore indicators of the fitting's capacity.

2.3. Applicable Measurements

A National Instruments data acquisition (DAQ) system served as the central platform for synchronizing and recording all experimental measurements. Sensors interfaced with the DAQ system captured parameters, including displacement, applied load, released water weight, and internal water pressure. Displacement measurements were obtained using Linear Variable Differential Transformer (LVDT) sensors of two types: the LWH Series (Figure 5a) and the LWG Rod-Type Series (Figure 5b). LWH Series were bonded to the pipe exterior to quantify relative displacement at the pipe-fitting interface, while the LWG sensors, magnetically mounted across adjacent pipes, measured the relative displacement between pipes. Figure 6 depicts the sensor layout in the vicinity of the fitting.

(**a**) (**b**)

Figure 5. Displacement Sensors: (**a**) LWH Series Linear Variable Differential Transformer Sensor Fitting; (**b**) LWG Series Linear Rot Type Series Sensor.

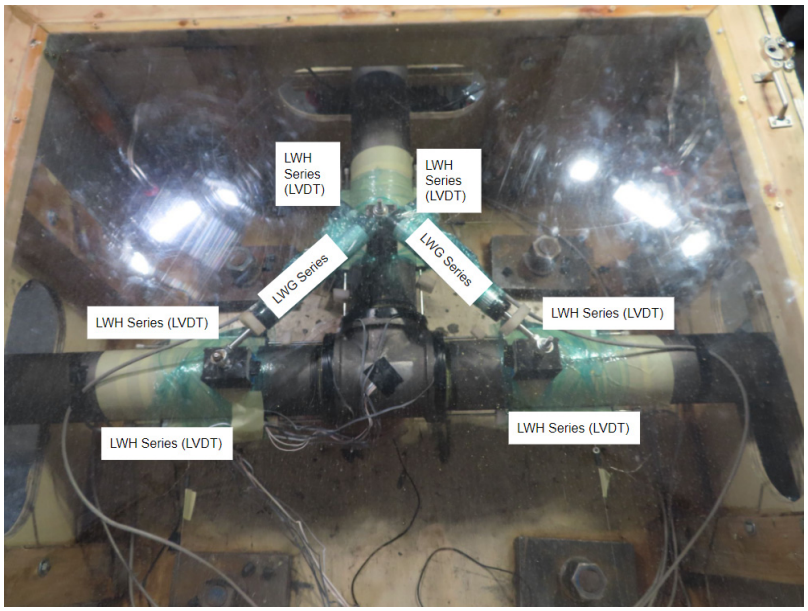

Figure 6. Displacement Sensors on and around the Fitting.

The servo-hydraulic actuator incorporated an internal LWH Series LVDT to monitor actuator stroke, as well as a calibrated load cell to measure the axial force imparted to the test assemblies. To quantify the mass of water discharged during each test, a high-precision platform-type load cell was positioned beneath the fitting. Water pressure within the system was monitored in real-time using a pressure transducer integrated with the DAQ system, supplemented by an analog pressure gauge installed directly on the test assembly for redundancy and verification.

2.4. Applicable Calculations

2.4.1. Bending Moment

The bending moment, denoted as M, was computed using the fundamental moment equation, expressed in Equation (1). In this equation, F is the applied force delivered by the servo-hydraulic actuator, and DA represents the corresponding moment arm:

$$M = F \times DA \quad (1)$$

The definition of the moment arm DA varied depending on the deformation behavior under consideration. For evaluations focused on pipe rotation, DA was defined as the distance from the actuator's point of load application to the outer face of the fitting. For assessments focused on fitting bending, DA was instead taken as the distance from the actuator's point of load application to the centroidal axis of the fitting.

2.4.2. Fitting Bending Calculations

The procedure used to calculate rotational capacity follows the methodology developed by Rusnak et al. [39], which accounts for the geometric relationships governing deformation within the fitting and adjacent pipe segments. For clarity, only the key steps and governing relationships are summarized herein, while the full derivation is available in the referenced work.

Table 2 lists the key variables used in the rotational capacity calculation procedure, while Figure 7 depicts the geometric parameters associated with fitting bending, adapted from Rusnak et al. [39], for both "push" and "pull" loading cycles. The underlying methodology remains consistent across both loading directions, with the only distinction occurring in the final angular computation. In Figure 7, the undeformed configuration is shown in black, the deformed configuration in red, and key geometric variables are highlighted in blue.

Table 2. Variables Associated with Fitting Bending Calculation (Adapted with permission from [39] © ASME).

Variable	Definition
a	Distance from the face of the fitting to the center of the fitting
D	Fitting-Joint hypotenuse after deformation
HYP	Fitting-Joint hypotenuse between the center of the LWG attachment points on the adjacent pipes prior to deformation
IIA	Initial internal angle of the undeformed fitting measured in the lab
Iθ_n	Internal angle present in fitting bending (βf) calculation
L	Distance from the face of the fitting to the center of the magnet that secured the LWG

Table 2. *Cont.*

Variable	Definition
LPT	Measured horizontal distance, in the horizontal plane, between the point of contact the LPS' (LVDT's) make on the face of the fitting
LWGr	Raw lab recording from the LWG displacement sensor
W	The distance from the center of the fitting to the center of the magnet fastening the LWG to the pipe
α	Pipe rotation
β	Fitting bending
ψ	Adjacent angle from α
ΔP	Manipulation sum of Iθ# present in the fitting bending (βf) calculation

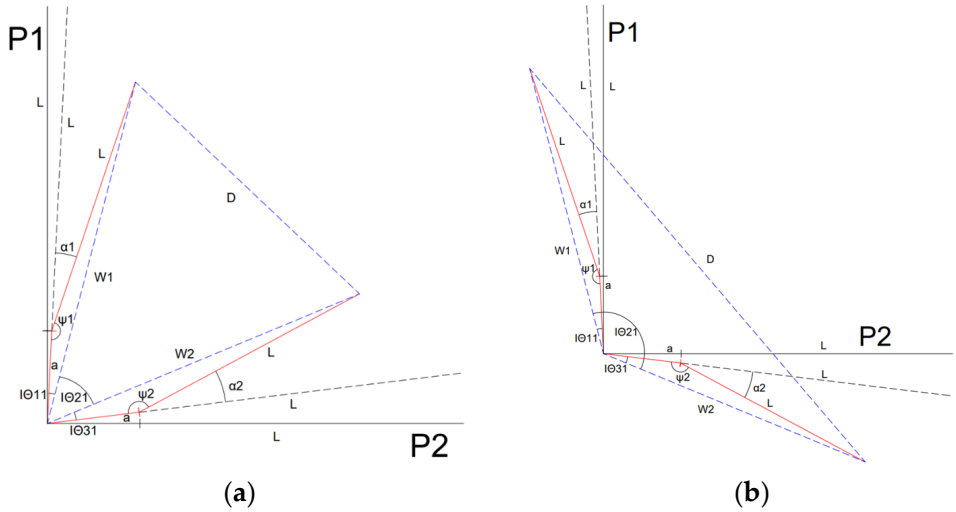

Figure 7. Deformation Shapes of an Elbow Regarding Fitting Bending: (**a**) Deformed Shape of an Elbow in a "Pull" Orientation; (**b**) Deformed Shape of an Elbow in a "Push" Orientation. Reprinted with permission from [39] © ASME.

The first step involves determining the pipe rotation angle, denoted as α, for each pipe segment using paired LVDT measurements positioned on opposite sides of the pipe. The rotation is computed based on the differential displacement across the pipe diameter, as defined in Equations (2)–(4). The parameter LPT represents the horizontal distance from the point of sensor contact on the fitting face to the pipe's longitudinal axis, as depicted in Figure 8, and is used in the calculation of pipe rotation. Equation (4), marked with an asterisk (*), is specific to tee configurations and does not apply to elbows.

$$\alpha 1 = tan^{-1}\left(\frac{LVDT1 + LVDT2}{LPT}\right) \quad (2)$$

$$\alpha 2 = tan^{-1}\left(\frac{LVDT3 + LVDT4}{LPT}\right) \quad (3)$$

$$\alpha 3 = tan^{-1}\left(\frac{LVDT5 + LVDT6}{LPT}\right) \quad (*\,4)$$

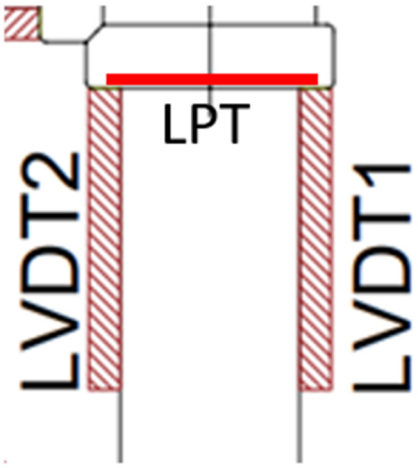

Figure 8. Depiction of LPT Location.

Using the calculated pipe rotations, the adjacent angles (ψ) are determined, followed by computation of the deformed geometry of the system. The deformed hypotenuse (D) is computed from the initial geometry and measured displacements (Equations (5)–(9)).

$$\psi 1 = 180 - \alpha 1 \tag{5}$$

$$\psi 2 = 180 - \alpha 2 \tag{6}$$

$$\psi 3 = 180 - \alpha 3 \tag{7}$$

$$D1 = HYP + LWG1r \tag{8}$$

$$D2 = HYP + LWG2r \tag{9}$$

The internal geometric configuration of the fitting is then evaluated using the derived segment lengths and angles. These relationships define the internal angles (Iθn), which characterize the deformation within the fitting (Equations (10)–(15)).

$$W1 = \sqrt{a^2 + L^2 - 2(a)(L)cos\psi 1} \tag{10}$$

$$W2 = \sqrt{a^2 + L^2 - 2(a)(L)cos\psi 2} \tag{11}$$

$$W3 = \sqrt{a^2 + L^2 - 2(a)(L)cos\psi 3} \tag{12}$$

$$I\theta 1 = sin^{-1}(L/(W1/sin\,\psi 1)) \tag{13}$$

$$I\theta 2 = cos^{-1}\left(\frac{W1^2 + W2^2 - D1^2}{2(W1)(W2)}\right) \tag{14}$$

$$I\theta 3 = sin^{-1}(L/(W2/sin\,\psi 2)) \tag{15}$$

The final fitting rotation (βf) is computed based on the resulting internal angles, accounting for differences between push and pull loading conditions (Equations (16)–(18)).

$$\Delta PL = I\theta 1 + I\theta 2 + I\theta 3 \tag{16}$$

$$\Delta PS = I\theta 2 - I\theta 1 + I\theta 3 \tag{17}$$

$$\beta f = IIA - \Delta P \tag{18}$$

3. Results

3.1. Physical Damages and Damage States of the Large Size Threaded Cast Iron Pipe Fittings

Figures 9–13 illustrate the observed deformation patterns and failure modes across the tested configurations and Table 3 provides an overview of their observed damage. Elbow fittings exhibited consistent behavior, with deformation occurring primarily in the adjoining pipe segments and no observable damage to the fitting body. In contrast, tee fittings demonstrated more complex responses, with failure typically initiating within the fitting itself. Fracture was frequently observed along the casting seam, indicating a likely material discontinuity associated with the manufacturing process. Additionally, 3-inch tee specimens occasionally exhibited visible leakage at the pipe–fitting interface prior to failure, whereas 4-inch fittings more frequently exhibited abrupt fracture without visible precursors. These observations highlight the influence of both fitting geometry and size on failure behavior.

Figure 9. Elbow Fitting Rupture Observed from Lab.

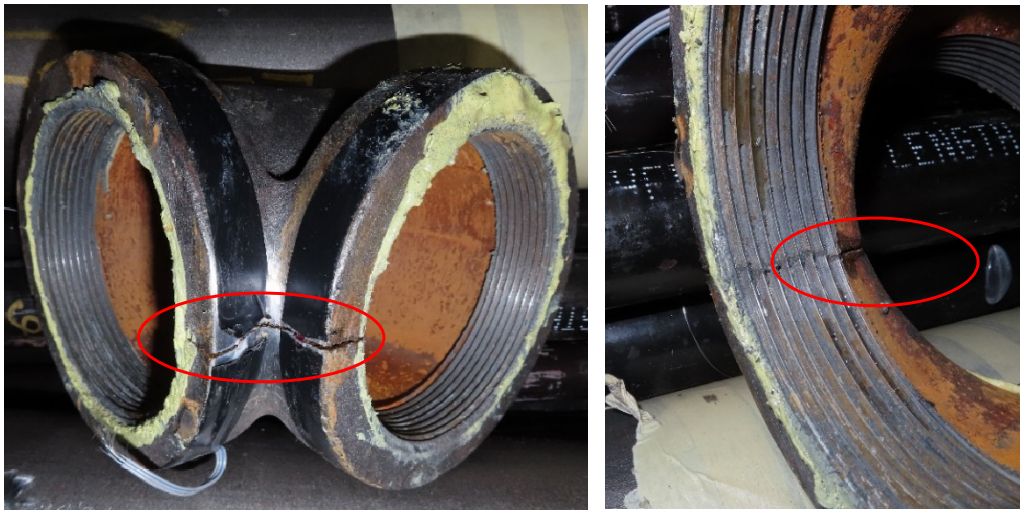

(**a**) (**b**)

Figure 10. Post Disassembly Elbow Fitting Fracture Images: (**a**) Fitting Rupture Along Casting Line; (**b**)Threads of the Fitting Post Rupture.

(**a**) (**b**)

Figure 11. Tee Fitting Rupture Observed in Lab: (**a**) Leakage Prior to Rupture; (**b**) Fitting Body Rupture.

(**a**) (**b**)

Figure 12. Post Disassembly Tee Fitting Body Rupture Images: (**a**) Body Rupture Outside of Fitting; (**b**) Body Rupture Inside of Fitting.

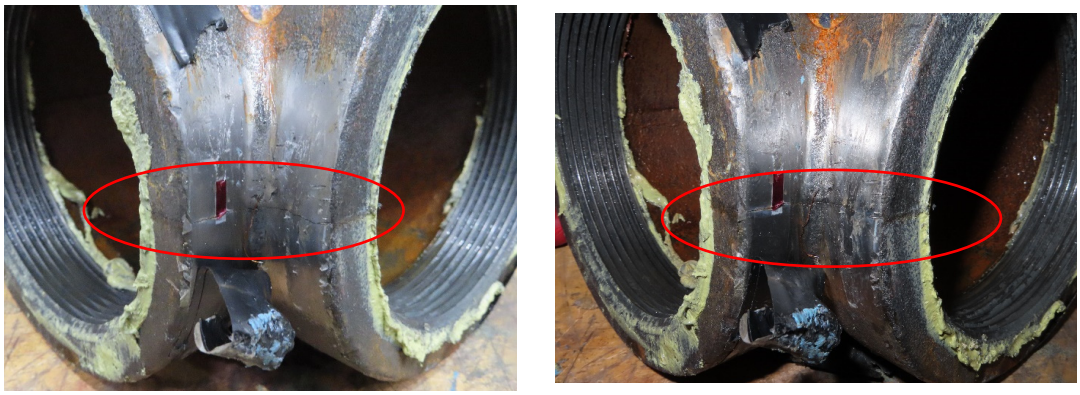

(**a**) (**b**)

Figure 13. Post Disassembly Tee Fitting Casting Line Rupture Images: (**a**) Casting Line Tee Rupture 1; (**b**) Casting Line Tee Rupture 2.

Table 3. Observed Damage and their Associated Descriptions.

Fitting Type/Configuration	Observed Damages and Description
Elbow	No detectable signs of early damage prior to failure;
	Catastrophic rupture occurred suddenly along the casting seam in both 3-inch and 4-inch elbow fittings (Figure 9)
Tee in Primary Configuration	Occasional early-stage leakage observed in 3-inch tee assemblies at the pipe-to-fitting interface (Figure 11a);
	In cases where leakage was present, a gradual increase in leakage occurred prior to rupture;
	4-inch tee assemblies exhibited no early leakage and failed suddenly without prior indication (Figure 11b)
Tee in Secondary Configuration	Similar to the primary configuration, early leakage was sporadically observed in 3-inch tee assemblies at the pipe-to-fitting interface;
	Leakage, when present, increased marginally prior to failure;
	4-inch tee assemblies demonstrated no precursory leakage and experienced sudden rupture

To enable direct comparison with prior testing on smaller-diameter fittings, the same damage state classification system established by Rusnak et al. [20] was adopted for this study, as detailed in Table 4. Each defined damage state represents a discrete threshold in the system's performance degradation. Notably, Damage States 2 (DS2) and 3 (DS3) were used as criteria for test termination, marking the onset of significant leakage and structural failure, respectively. The transition between DS1 and DS3 was limited, as most configurations exhibited abrupt rupture with little to no intermediate damage progression. Only select 3-inch tee configurations demonstrated observable leakage prior to failure, while the remaining configurations transitioned directly to structural rupture.

Table 4. Damage States List and their Associated Description.

Damage State	Damage State Description
DS1	Onset of leakage, visually detected at the pipe-fitting interface
DS2	Accumulation of 2 oz of water during testing
DS3	Structural failure of the fitting or adjoining pipe segment

3.2. Rotational Capacity of the Large Size Threaded Cast Iron Pipe Fittings

Rotational capacities corresponding to the defined damage states (as listed in Table 4) were quantified for each fitting size and configuration. These capacities were obtained by averaging results from three (3) tests per configuration. Two rotational metrics were evaluated: (1) rotation of the fitting itself (fitting bending), and (2) rotation of the loading pipe relative to the face of the fitting (pipe rotation). For elbow configurations, the rotations measured at both connected pipes (Pipe 1 and Pipe 2) were averaged due to their symmetric characteristics. The computed rotational capacities for fitting rotation and pipe rotation are depicted in Figures 14 and 15, respectively, in the form of comparative bar charts. In both figures, subsection (A) corresponds to elbow assemblies, subsection (B) to tees loaded in the primary configuration, and subsection (C) to tees in the secondary configuration. The damage states are color-coded, with DS1 denoted in blue and DS3 in gray. 4-inch fittings exhibited greater rotational capacity at DS3 compared to their 3-inch counterparts. However, the 3-inch configurations demonstrated consistently higher pipe rotations across all damage states. It is important to note that Damage State 2 (DS2) was

not observed in any test configuration. Among all configurations tested, elbows exhibited the highest rotational capacities, significantly exceeding those of the tee fittings. Tee assemblies displayed comparable rotational behavior between the primary and secondary loading configurations.

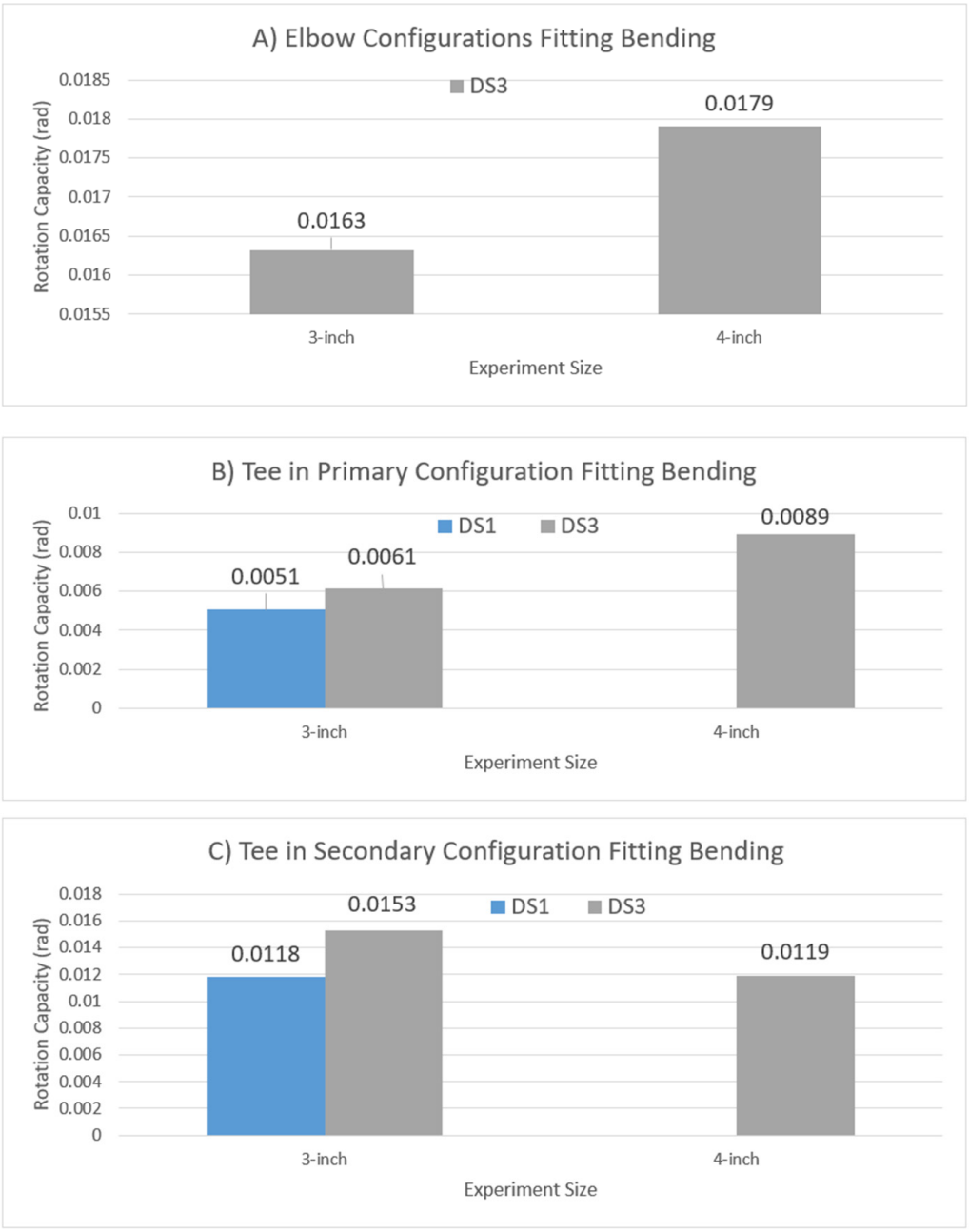

Figure 14. Measured Rotational Capacity of the Fitting (Fitting Bending): (**A**) Elbow Configuration; (**B**) Tee in Primary Configuration; (**C**) Tee in Secondary Configuration (Unit: rad).

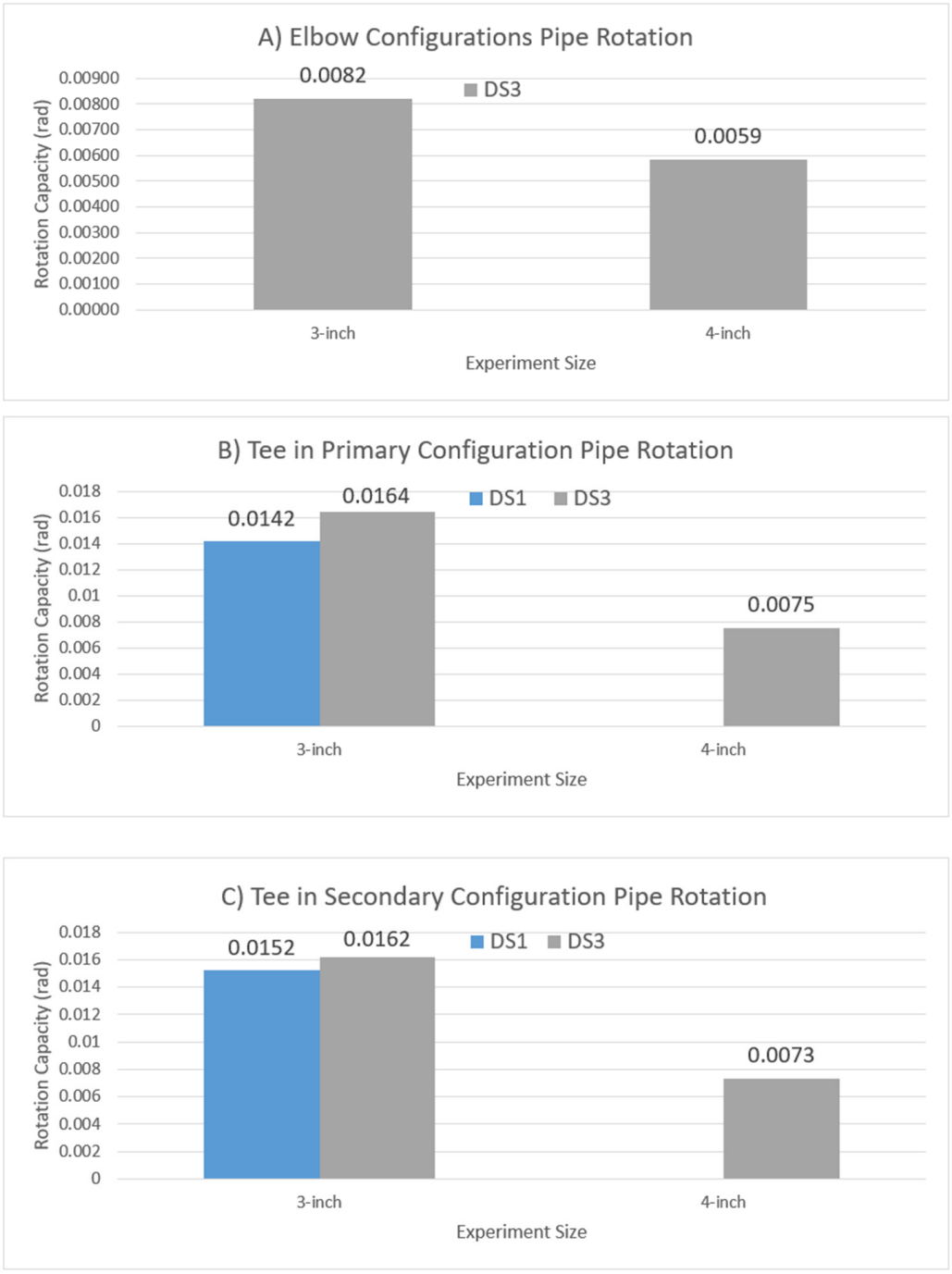

Figure 15. Measured Rotational Capacity of the Pipe About the Face of the Fitting (Pipe Rotation): (**A**) Elbow Configuration; (**B**) Tee in Primary Configuration; (**C**) Tee in Secondary Configuration (Unit: rad).

3.3. Moment vs. Rotation Response of the Large Size Threaded Cast Iron Pipe Fittings

Figures 16–21 illustrate the moment–rotation hysteresis loops for each tested assembly, providing insight into both the cyclic performance and progressive degradation of the pipe-fitting assemblies under the applied loading.

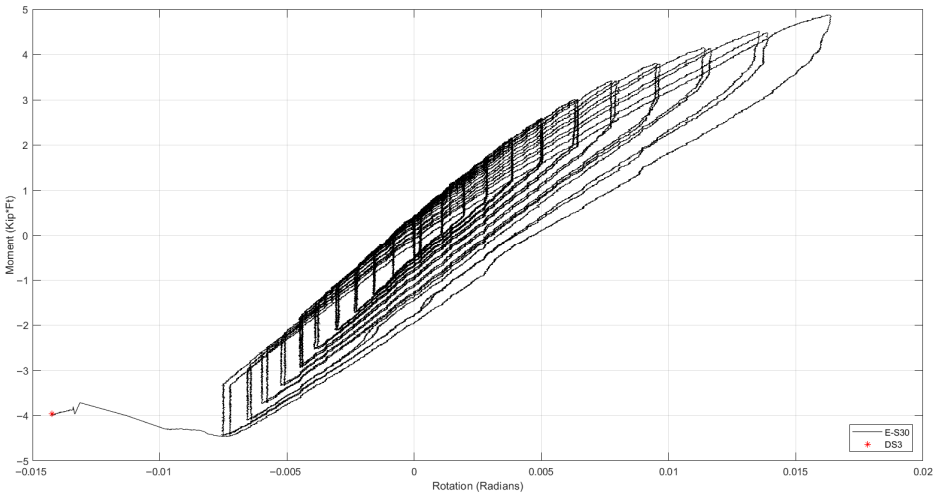

(**a**)

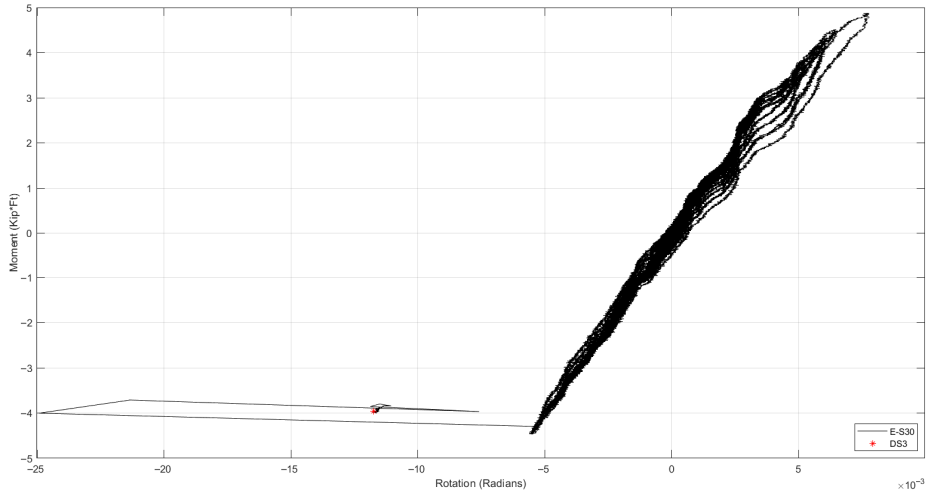

(**b**)

Figure 16. The 3-inch Elbow Hysteresis Loops: (**a**) Behavior in the Fitting; (**b**) Behavior of the Loading Pipe.

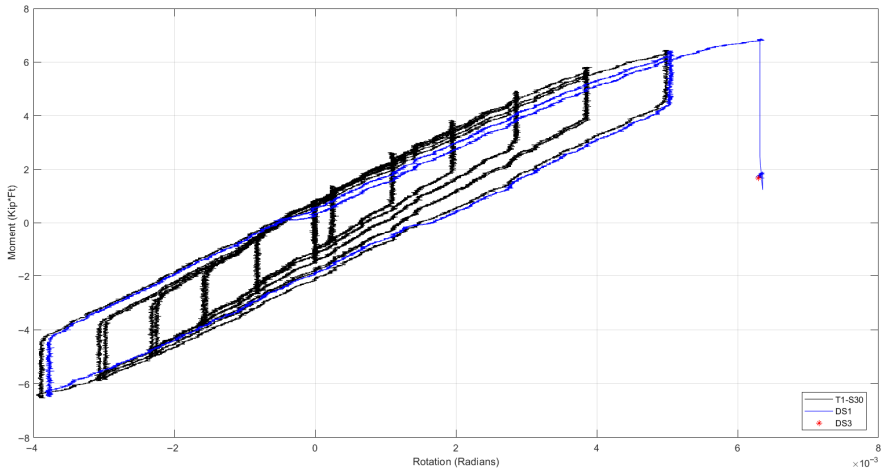

(**a**)

Figure 17. *Cont.*

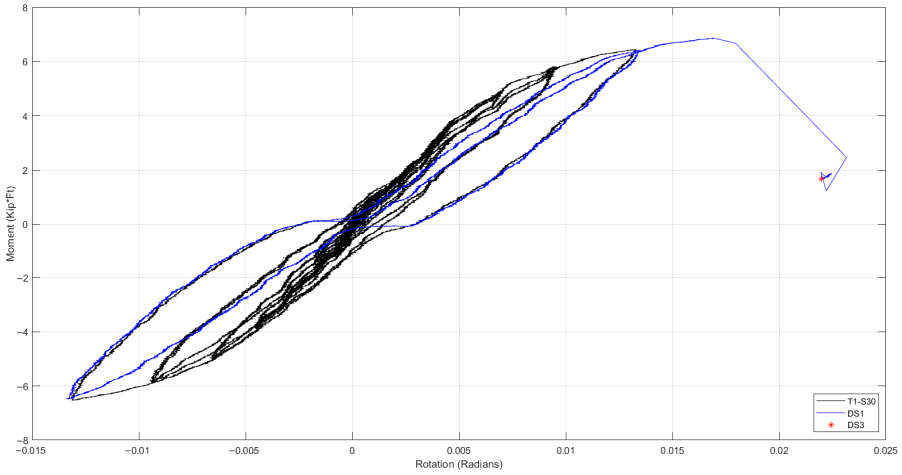

(**b**)

Figure 17. The 3-inch Tee Primary Hysteresis Loops: (**a**) Behavior in the Fitting; (**b**) Behavior of the Loading Pipe.

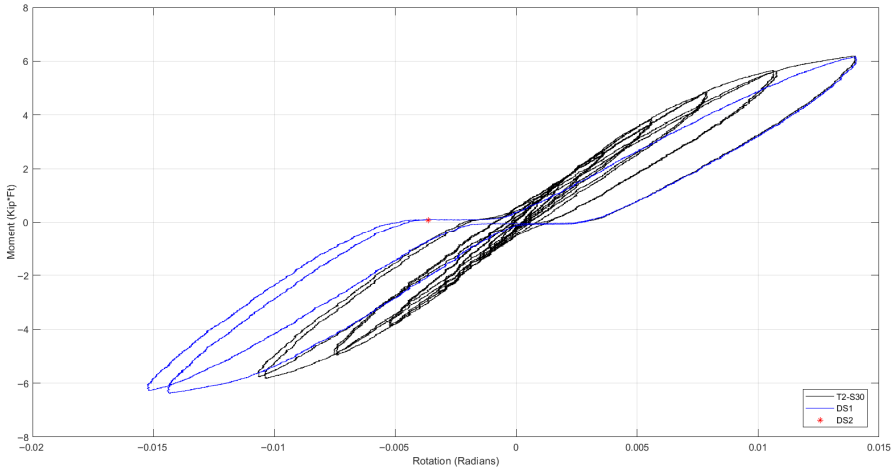

(**a**)

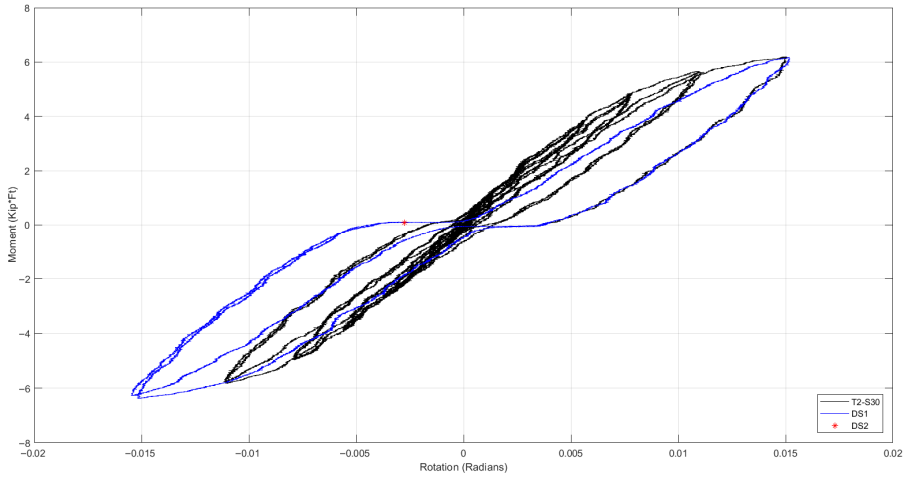

(**b**)

Figure 18. The 3-inch Tee Secondary Hysteresis Loops: (**a**) Behavior in the Fitting; (**b**) Behavior of the Loading Pipe.

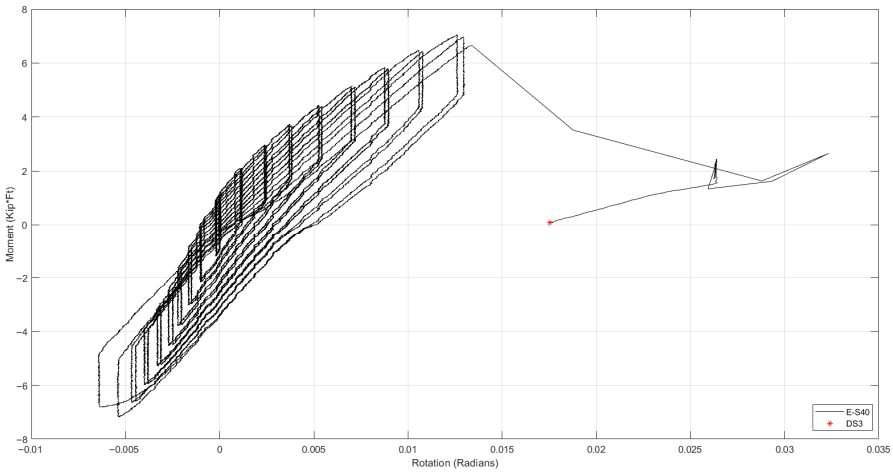

(**a**)

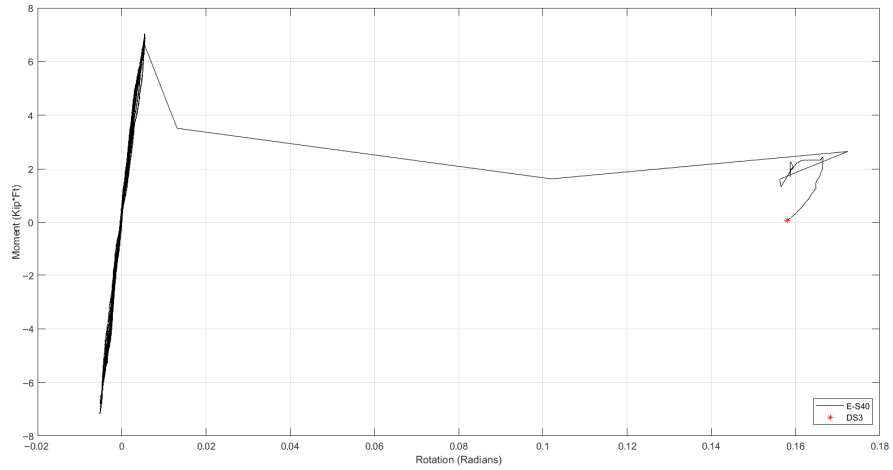

(**b**)

Figure 19. The 4-inch Elbow Hysteresis Loops: (**a**) Behavior in the Fitting; (**b**) Behavior of the Loading Pipe.

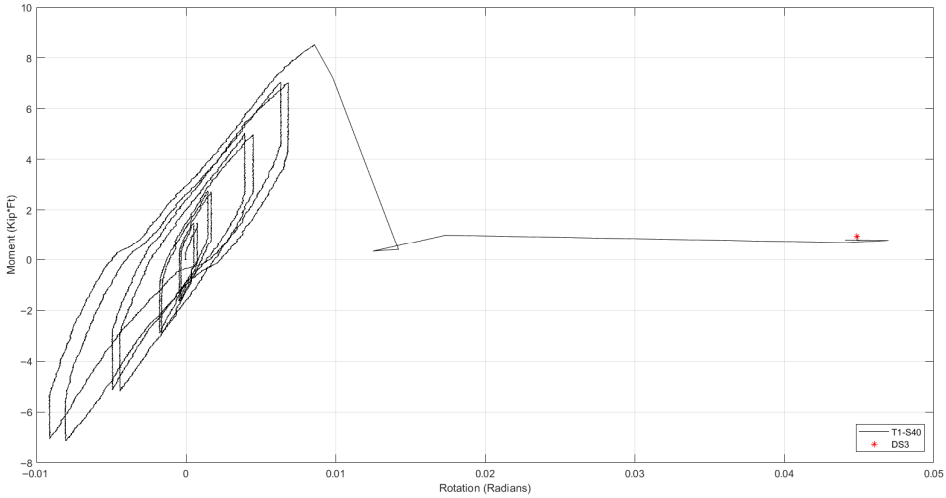

(**a**)

Figure 20. *Cont.*

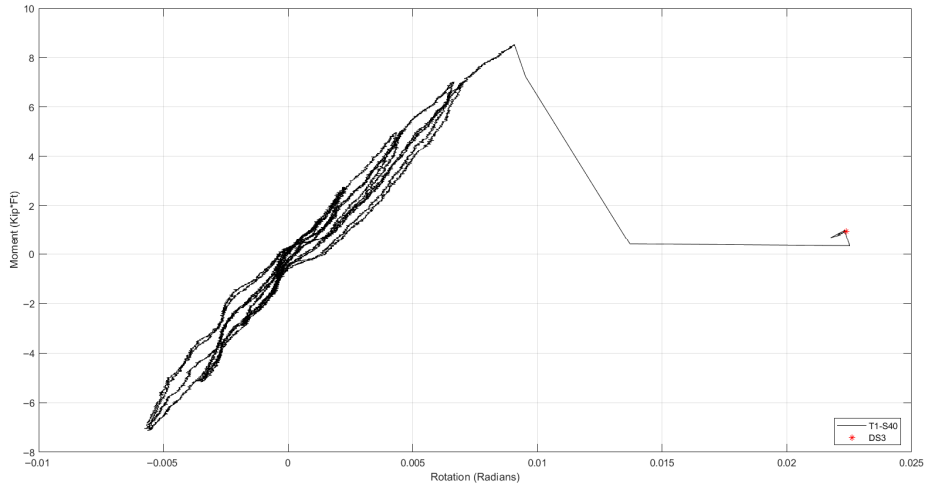

(**b**)

Figure 20. The 4-inch Tee Primary Hysteresis Loops: (**a**) Behavior in the Fitting; (**b**) Behavior of the Loading Pipe.

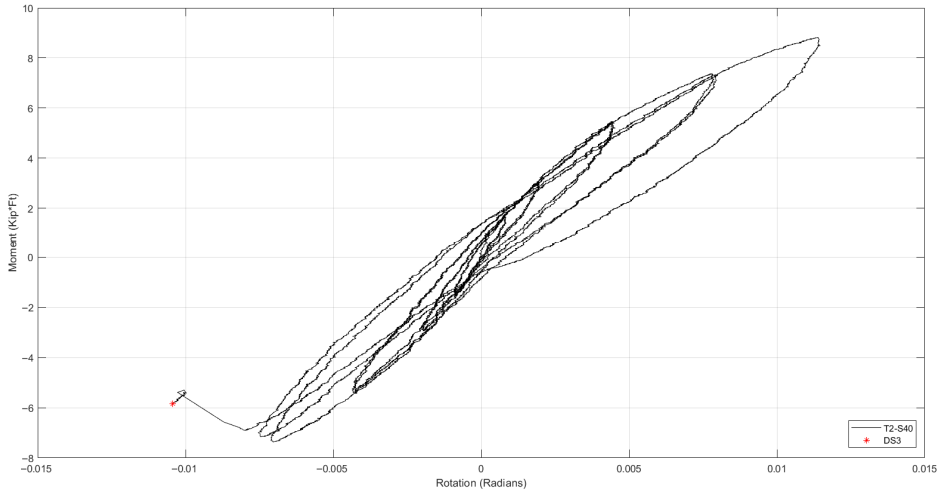

(**a**)

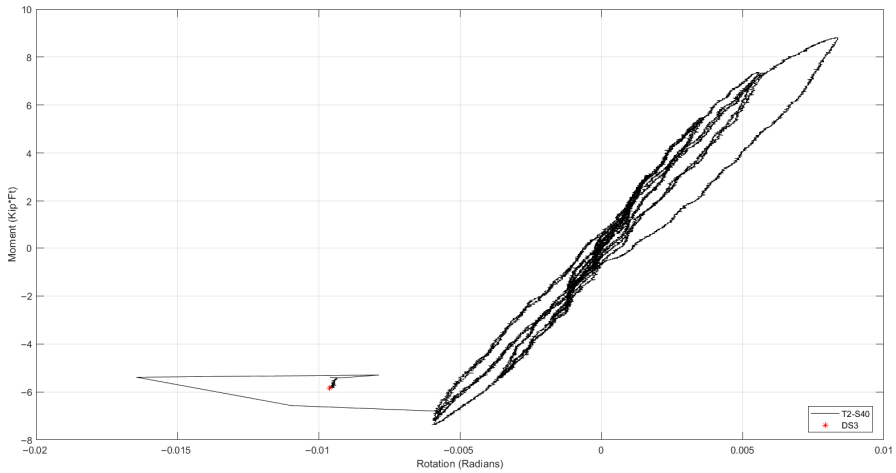

(**b**)

Figure 21. The 4-inch Tee Secondary Hysteresis Loops: (**a**) Behavior in the Fitting; (**b**) Behavior of the Loading Pipe.

Quantitatively, the moment–rotation response of the tested assemblies exhibits clear trends with respect to fitting size and configuration. The average peak moments ranged from approximately 4.9 kip-ft for 3-inch elbow configurations to 8.7 kip-ft for 4-inch tee configurations. Corresponding rotational capacities at failure ranged from approximately 0.006 to 0.018 radians. These values indicate increased moment capacity and reduced rotational capacity with increasing fitting size, consistent across the tested configurations.

Figures 16–18 correspond to the 3-inch assemblies, while Figures 19–21 represent the 4-inch assemblies. Each plot presents two distinct rotational responses: the rotation attributed to fitting deformation (fitting bending) and the rotation of the loading pipe (pipe rotation). Solid black curves denote loading cycles prior to the onset of any observable damage. The initiation of the blue curve signifies the occurrence of Damage State 1 (DS1), corresponding to the first detectable leakage. A red star marks the termination point of each test, which coincides with Damage State 3 (DS3), representing structural failure of the fitting or pipe. Moment values were calculated based on Equation (1), and the corresponding rotations were determined in accordance with the methodology outlined in the Applicable Calculations section. Table 5 summarizes the maximum moment demand, peak rotation, and corresponding rotational capacities for both fitting bending and pipe rotation across all test configurations.

Table 5. Maximum Moment, Rotation and Rotational Capacity.

Size (inch)	Configuration	Fitting Bending (β)			Pipe Rotation (α)		
		M (kip-ft)	Rotation (rad)	Capacity (kip-ft per rad)	M (kip-ft)	Rotation (rad)	Capacity (kip-ft per rad)
3	Elbow	4.94	0.0163	303.1	4.94	0.0082	602.4
	Tee Primary	6.46	0.0061	1059.0	6.46	0.0164	393.9
	Tee Secondary	6.22	0.0153	406.5	6.22	0.0162	384.0
4	Elbow	7.19	0.0179	401.7	7.19	0.0059	1218.6
	Tee Primary	8.52	0.0089	957.3	8.52	0.0075	1136.0
	Tee Secondary	8.71	0.0119	731.9	8.71	0.0073	1193.2

3.4. Fragility Analysis of the Large Size Threaded Cast Iron Pipe Fittings

Fragility analysis provides a probabilistic framework for quantifying the likelihood that a component will reach or exceed a defined damage state under a given demand parameter. In this study, rotational demand is used as the engineering demand parameter (EDP), and fragility functions are developed to characterize the probability of exceeding each defined damage state. A lognormal distribution is adopted, consistent with established methodologies in performance-based earthquake engineering, to represent the variability in the experimental response. The lognormal distribution was selected due to its widespread use in fragility analysis and its suitability for representing positive response parameters such as rotational capacity.

The experimental data were analyzed to construct seismic fragility models specific to threaded cast iron fittings. Across all sizes and configurations, the dominant parameter influencing the fittings' response was identified as structural failure (or rupture), which was selected as the primary engineering demand parameter (EDP) for the fragility assessment, while leakage was considered as an additional damage state where observed. To characterize the probability of reaching each damage state, a statistical framework consistent with FEMA P58 [40] and the methodology proposed by Porter et al. [41] was employed. Fragility functions were developed for the observed damage states (DS1 and DS3) for all applicable configurations, as shown in Figures 14 and 15. Each fragility function, denoted F(θ), was defined by Equation (19), where φ is the standard normal cumulative distribution function,

θ_m is the median rotational capacity for a given damage state, and β is the logarithmic standard deviation.

$$F(\theta) = \varphi\left(\frac{ln(\theta/\theta_m)}{\beta}\right) \quad (19)$$

The parameters θ_m and β were computed using Equations (20)–(22). Here, θi represents the rotational capacity from the i-th test, and M is the total number of specimens tested for a given fitting size (in this study, M = 3). To account for the limited sample size and the variability in component condition, an additional uncertainty term, $\beta_u = 0.25$, was incorporated into the total logarithmic standard deviation, following the recommendations of FEMA P58 [40] and Porter et al. [41].

$$\theta_m = e^{\left(\frac{1}{M}\sum_{i=1}^{M} ln(\theta_i)\right)} \quad (20)$$

$$\beta_t = \sqrt{\frac{1}{M-1}\sum_{i=1}^{M}\left(ln\left(\frac{\theta_i}{\theta_m}\right)\right)^2} \quad (21)$$

$$\beta = \sqrt{\beta_t^2+\beta_u^2} \quad (22)$$

A summary of the experimental outcomes is provided in Table 6, and the corresponding fragility curves are shown in Figures 22–24. Figure 22 depicts the fragility curves for the elbow fittings, Figure 23 illustrates the fragility curves for the tee fittings tested in the primary configuration, and Figure 24 presents the results for those tested in the secondary configuration. It should be emphasized that the number of specimens tested in this study is limited, and while the results provide valuable insight into the behavior of large-diameter fittings, additional testing is necessary to improve statistical confidence and more comprehensively evaluate the influence of geometric parameters, material variability, and system conditions on the resulting fragility relationships.

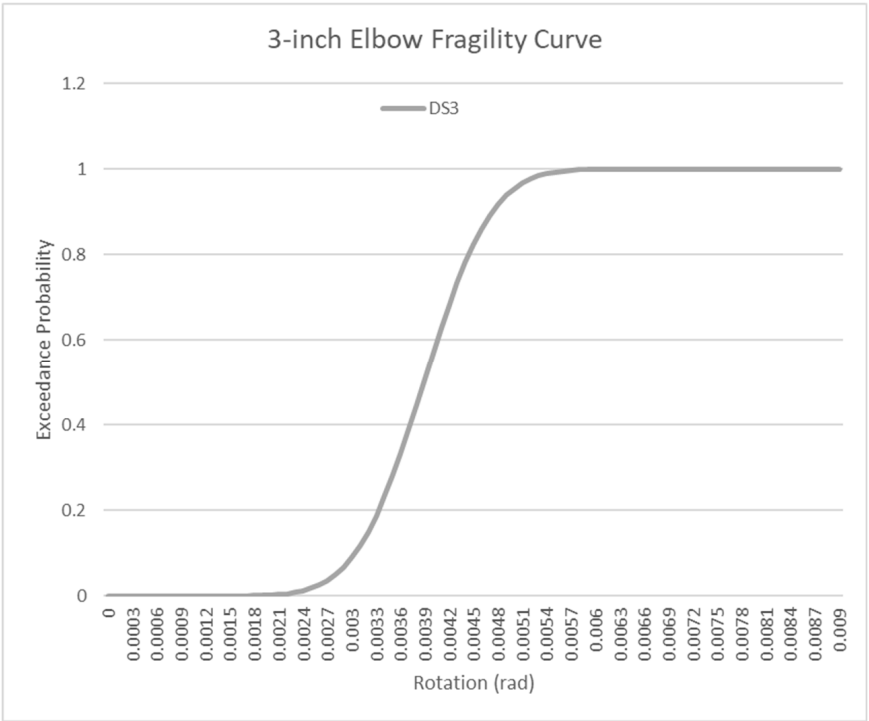

(**a**)

Figure 22. *Cont.*

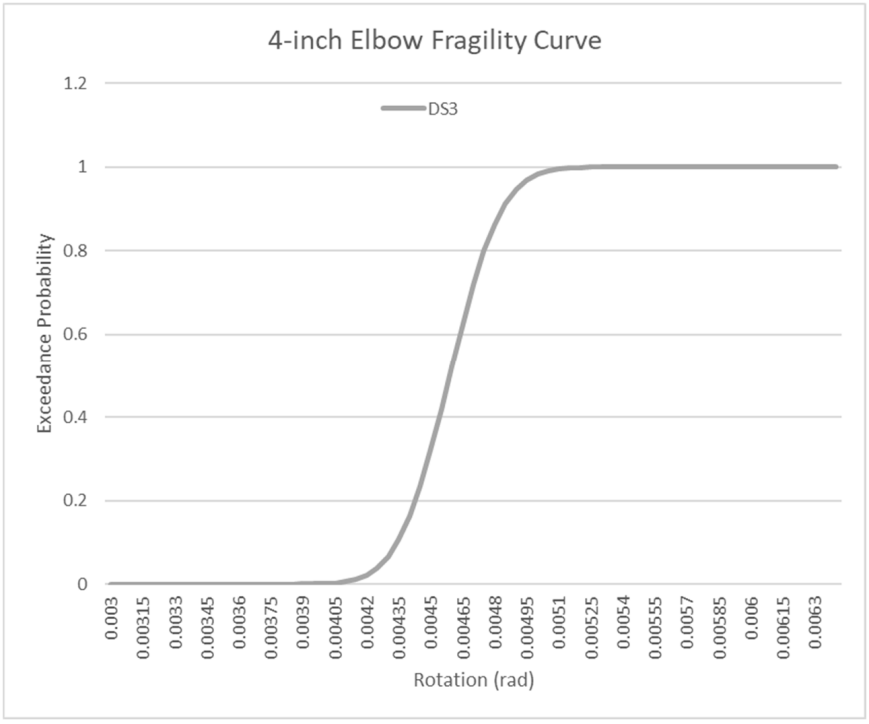

(**b**)

Figure 22. Elbow Configuration Fragility Curves: (**a**) 3-inch; (**b**) 4-inch.

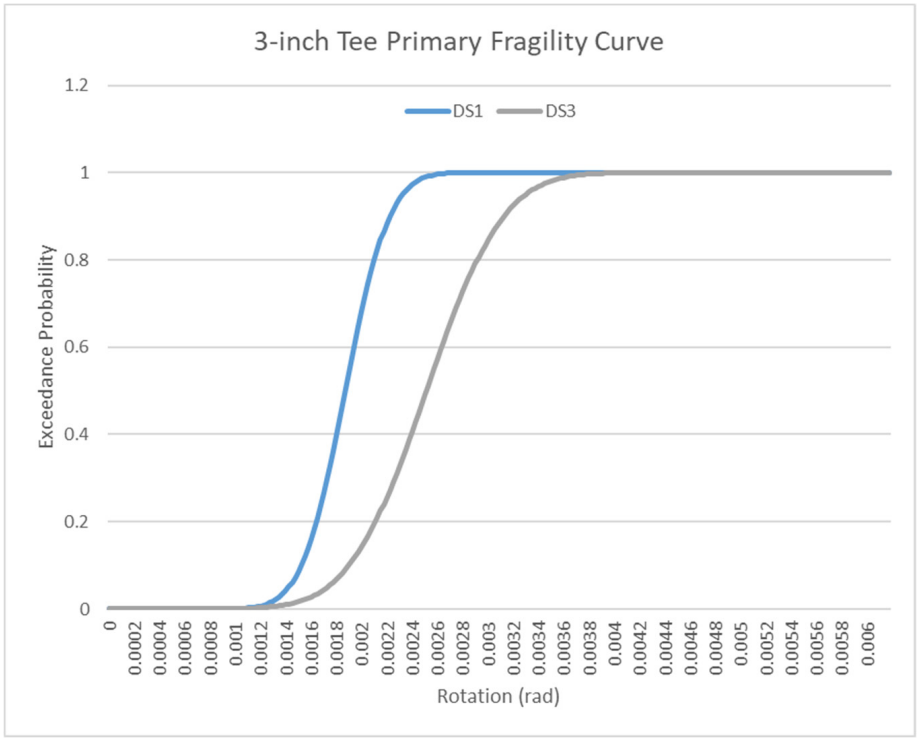

(**a**)

Figure 23. *Cont.*

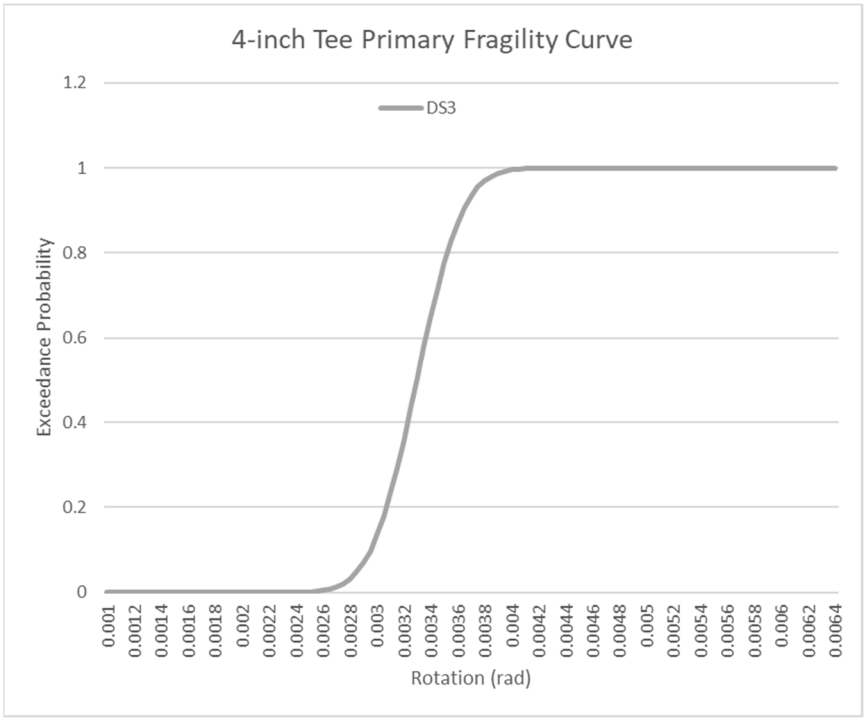

(**b**)

Figure 23. Tees in the Primary Configuration Fragility Curves: (**a**) 3-inch; (**b**) 4-inch.

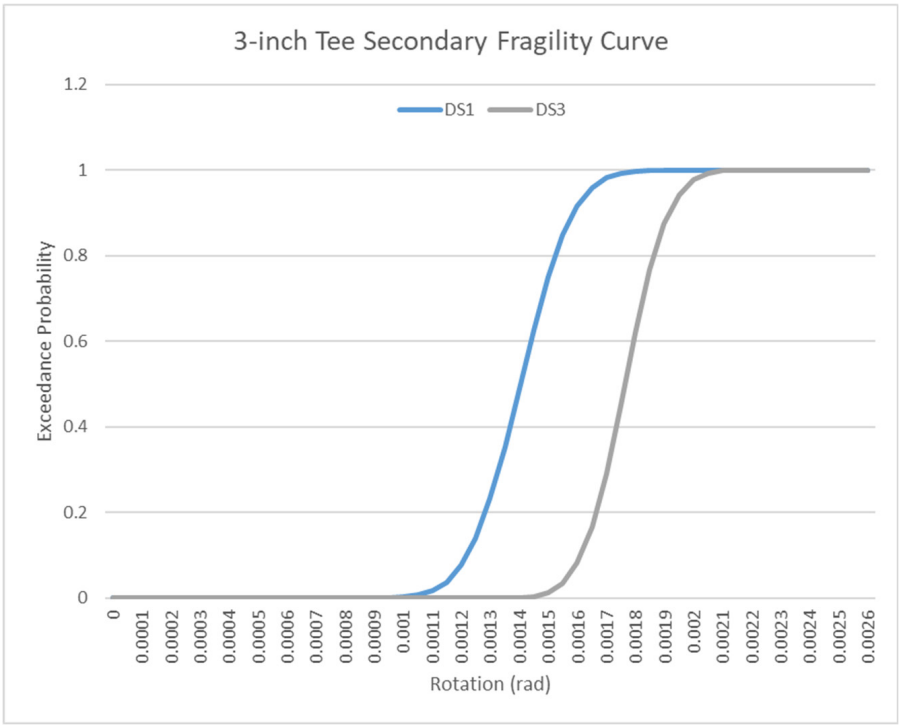

(**a**)

Figure 24. *Cont.*

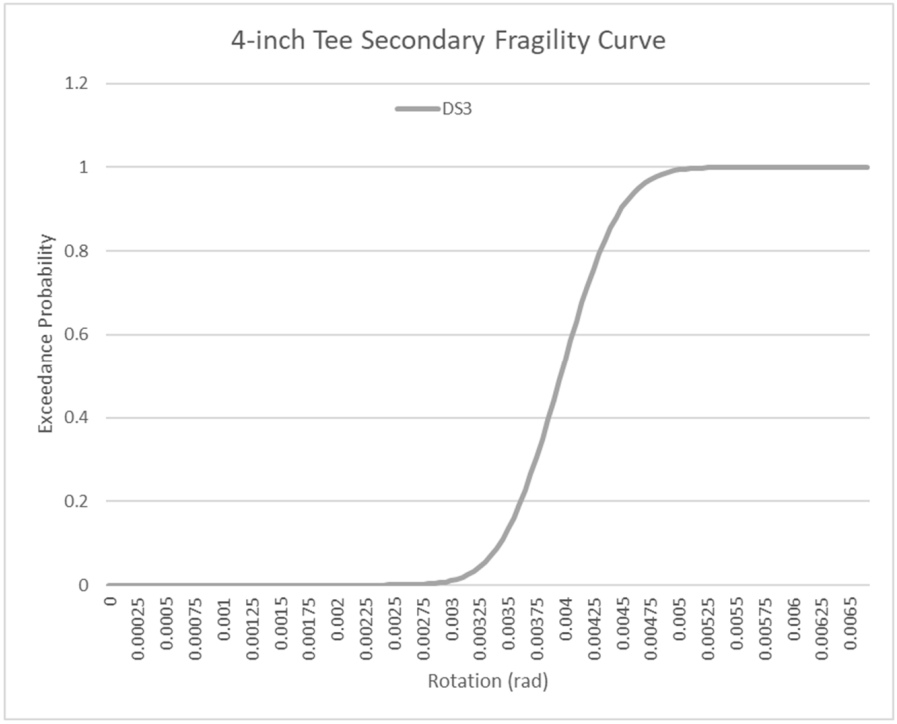

(**b**)

Figure 24. Tees in the Secondary Configuration Fragility Curves: (**a**) 3-inch; (**b**) 4-inch.

Table 6. Summary of Fragility Parameters of the Larger Size Threaded Cast Iron Fittings.

	Configuration	Size (inch)	DS1		DS3	
			θm (rad)	β	θm (rad)	β
Beta (β)	Elbow	3	N/A		0.0039	0.2990
		4			0.0046	0.2536
	TP	3	0.0019	0.2928	0.0025	0.3549
		4	0.0014	0.2709	0.0033	0.2624
	TS	3	N/A		0.0018	0.2590
		4			0.0039	0.2702

4. Discussion

A total of 18 large-diameter threaded cast iron pipe-fitting assemblies, comprising both 3-inch and 4-inch elbows and tees, were subjected to quasi-static loading to evaluate their rotational capacities and develop seismic fragility models. The key findings and comparative insights are summarized as follows:

(1) Across all tested configurations, structural rupture of the fitting body was the dominant failure mode, corresponding to Damage State 3 (DS3). Leakage corresponding to DS1 was observed only in the 3-inch tee assemblies; no specimen exhibited the substantial leakage defined as DS2.

(2) Maximum rotational capacities of the fittings ranged from 0.0063 to 0.0179 radians, measured at the fitting body. Corresponding pipe rotations, measured at the face of the fitting, ranged from 0.0059 to 0.0082 radians, both indicative of DS3. Pipe rotations showed minimal variation between tee loading configurations.

(3) Moment–rotation hysteresis loops revealed distinct behavioral signatures. Most assemblies displayed cyclic responses until abrupt rupture. The transition to DS3 was characterized by a sudden drop in moment capacity following peak moments

on the order of 4.9 to 8.7 kip-ft, depending on configuration. Notably, the 3-inch tee assemblies were the only cases to show progressive leakage (DS1) prior to rupture.

(4) The fragility models derived from the test data incorporate the logarithmic standard deviation (β) to quantify uncertainty in the rotational capacity. This dispersion accounts for material variability, dimensional tolerances, and assembly imperfections. The β values were comparable across fitting sizes, suggesting consistent variability irrespective of nominal diameter. The use of β in the probabilistic framework enables performance predictions under a broader range of seismic demands and enhances the reliability of the fragility analysis.

(5) As depicted in Figures 22–24, the fragility curves demonstrate a higher susceptibility to damage initiation in 3-inch fittings, which reached defined damage states at lower rotation levels compared to 4-inch fittings. This suggests that, despite their smaller size, 3-inch fittings may be more vulnerable under seismic deformation demands. No significant differences were observed between tee configurations regarding their damage probabilities.

(6) Comparative analysis with the prior study by Rusnak et al. [20], which investigated smaller fittings (1–2 inches), revealed several important trends:

   (a) Smaller fittings exhibited greater rotational capacity before reaching any damage state.
   (b) No failure was observed in elbows up to 2 inches in the earlier study, contrasting with the rupture observed in both 3- and 4-inch elbows in this study.
   (c) In smaller fittings, pipe rotation and fitting bending decreased with size, while in the larger sizes examined here, fitting bending capacity increased with size, but pipe rotation slightly decreased. In all cases, pipe rotation exceeded fitting bending.
   (d) Hysteresis loops for smaller fittings displayed more gradual degradation, whereas those for larger fittings exhibited an abrupt rupture pattern.
   (e) While the defined EDPs differed between the studies, relative comparisons suggest that smaller fittings tolerated greater deformation at the fitting face before reaching damage thresholds.

5. Conclusions

This experimental investigation of 18 large-diameter threaded cast iron pipe-fitting assemblies has demonstrated the considerable structural capacity of fire suppression systems utilizing cast iron fittings. The results indicate that these assemblies can withstand deformation before any damage occurs, with the forces and moments required to initiate failure exceeding those imposed during the experimental loading protocol and suggesting substantial capacity relative to typical service-level demands. Such resilience underscores the robustness of these systems in the face of extreme loading scenarios. The fragility assessment incorporated a probabilistic framework to quantify the uncertainty in rotational capacities at various damage states using the logarithmic standard deviation (β). These β-values proved valuable in capturing variability due to factors such as material inconsistencies and assembly tolerances, supporting the development of reliable fragility models for seismic applications. The modeling approach presented enables engineers to evaluate not only the median performance of fire suppression components but also the probabilistic distribution of their behavior under seismic loading.

The findings underscore a size-dependent mechanical response, with 3-inch fittings demonstrating reduced rotational tolerance within the fitting body prior to damage compared to 4-inch fittings. In contrast, greater pipe rotation was observed in the 3-inch assemblies before reaching critical damage, indicating enhanced rotational flexibility at

the pipe–fitting interface. When viewed alongside prior data for fittings 2 inches and smaller (Rusnak et al. [20]), the current results mark a notable shift in behavior: leakage was the dominant failure mode for smaller fittings, while structural rupture governed the performance of 3-inch and 4-inch assemblies, indicating a stiffening effect as diameter increases. Across the typical fitting size range (1 to 4 inches), components smaller than 3 inches generally accommodate larger displacements and angular deformations. Probabilistic fragility results indicate that 3-inch fittings are more susceptible to failure at lower rotational inputs than their 4-inch counterparts. Importantly, the rotations associated with failure exceed commonly accepted interstory drift ratios (e.g., 2.5% of story height [42]), affirming the capacity of these fittings to sustain substantial deformation under seismic loading, provided they are allowed freedom of movement within the horizontal plane. Despite the brittle nature of cast iron, the overall system benefits from the rotational compliance introduced by threaded joint interactions, contributing to enhanced deformation capacity under lateral loading.

This investigation contributes to the broader understanding of the mechanical performance of threaded cast iron fittings used in fire suppression systems. Through quantification of rotational capacities and observed damage progression, this study establishes moment–rotation response curves specific to various fitting sizes and configurations. These empirical curves serve as critical input for the analytical modeling of threaded piping systems, capturing both the deformation capacity and failure characteristics of the fittings. Complementing this, the fragility assessment enables a probabilistic evaluation of failure likelihood across a spectrum of rotational demands, offering insights into the seismic resilience and structural reliability of these components in practical applications. Building on these findings, future efforts will extend the experimental scope to examine additional performance-influencing parameters, such as geometric variability, loading orientation, material aging, and multi-axial stress states, thereby advancing the predictive modeling and design guidance for cast iron fire suppression assemblies.

Author Contributions: Conceptualization, C.R. and S.E.; methodology, C.R., S.E. and A.R.; Software, C.R. and A.R.; validation, C.R. and S.E.; formal analysis, C.R. and A.R.; investigation, C.R., S.E. and A.R.; resources, C.R. and S.E.; data curation, C.R., S.E. and A.R.; writing—original draft preparation, C.R.; writing—review & editing, C.R., S.E. and A.R.; visualization, C.R., S.E. and A.R.; supervision, C.R. and S.E.; project administration, S.E.; funding acquisition, S.E. All authors have read and agreed to the published version of the manuscript.

Funding: This research was funded by the Los Alamos National Laboratory under subcontract number C1767 (Requisition CW17935). Any findings, conclusions and opinions presented are those of the authors and do not reflect the views of the sponsor.

Data Availability Statement: All processed data supporting the findings of this study are included within the article. The data generated and analyzed in this study is available from the corresponding author upon reasonable request.

Conflicts of Interest: The authors declare no conflict of interest.

References

1. Gillengerten, J. Design of Nonstructural System and Components. In *The Seismic Design Handbook*, 2nd ed.; Springer: New York, NY, USA, 2001.
2. Fleming, R.P. *Analysis of Fire Sprinkler Systems Performance in the Northridge Earthquake*; National Institute of Standards and Technology: Gaithersburg, MD, USA, 1998; NIST-GCR-98–736.
3. Baird, A. *Building Better—The Importance of Non-Structural Elements in Earthquakes*; BECA: Auckland, New Zealand, 2020.
4. Ayres, J.M.; Ezer Associates Inc. *Northridge Earthquake Hospital Water Damage Study*; Office of Statewide Health Planning and Development: Sacramento, CA, USA, 1996.

5. OSHPD. *Seismic Compliance Program and Product Report in Accordance with Assembly Bill 100*; Office of Statewide Health Planning and Development: Sacramento, CA, USA, 2021.
6. NIST. *Northridge Earthquake Performance of Structures, Lifelines, and Fire Protection Systems*; NIST Special Publication 862; National Institute of Standards and Technology: Gaithersburg, MD, USA, 1994.
7. OSHPD. *The Northridge Earthquake: A Report to the Hospital Building Safety Board on the Performance of Hospitals*; Office of Statewide Health Planning and Development: Sacramento, CA, USA, 1995.
8. Mizutani, K.; Kim, H.; Kikuchihara, M.; Nakai, T.; Nishino, M.; Sunouchi, S. The Damage of the Building Equipment Under the 2011 Tohoku Pacific Earthquake. In Proceedings of the 9th International Conference on Urban Earthquake Engineering and 4th Asia Conference on Earthquake Engineering, Tokyo, Japan, 6–8 March 2012.
9. Building Performance. *Practice Advisory 19: Improving Earthquake Performance of Non-Structural Elements*; Ministry of Business, Innovation & Employment: Wellington, New Zealand, 2016.
10. Kehoe, K. *Revisiting Earthquake Lessons—Nonstructural Components*; Structural Engineers Association of California: San Francisco, CA, USA, 2019.
11. Mulchandani, H.; Robertson, I.; Correa, T.; Prevatt, D.; Roueche, D.; Mosalam, K.; Achiari, H.; Esteban, M.; Krautwald, C.; Mikami, T.; et al. *StEER: Structural Extreme Event Reconnaissance Network Palu Earthquake and Tsunami, Sulawesi, Indonesia Field Assessment Team 1 (FAT-1) Early Access Reconnaissance Report (EARR)*; University of Notre Dame: Notre Dame, IN, USA, 2019. [CrossRef]
12. Wang, T.; Shang, Q.; Chen, X.; Li, J. Experiments and Fragility Analyses of Piping Systems Connected by Grooved Fit Joints with Large Deformability. *Front. Built Environ.* **2019**, *5*, 49. [CrossRef]
13. Tian, Y.; Filiatrault, A.; Mosqueda, G. *Experimental Seismic Study of Pressurized Fire Sprinkler Piping Subsystems*; MCEER-13-0001; University at Buffalo: Buffalo, NY, USA, 2013.
14. Zaghi, A.E.; Maragakis, E.M.; Itani, A.; Goodwin, E. Experimental and Analytical Studies of Hospital Piping Assemblies Subjected to Seismic Loading. *Earthq. Spectra* **2012**, *28*, 367–384. [CrossRef]
15. Qu, Z.; He, S.W.; Ye, L.H. Seismic Fragility of Water Supply Pipelines under Static and Dynamic Cyclic Loading. In Proceedings of the Huixian International Forum on Earthquake Engineering for Young Researchers, Huixian, China, 21–22 August 2018.
16. Antaki, G.; Gutierrez, B. Seismic Capacity of Threaded, Brazed and Grooved Pipe Joints. In Proceedings of the DOE Natural Phenomena Hazards Workshop, Germantown, MD, USA, 25–26 October 2011.
17. Antaki, G.; Guzy, D. Seismic Testing of Grooved and Threaded Fire Protection Joints and Correlation with NFPA Seismic Design Provisions. In Proceedings of the ASME Pressure Vessels and Piping Division, San Diego, CA, USA, 26–30 July 1998; Volume 364, pp. 69–75.
18. Soroushian, S.; Zaghi, A.E.; Maragakis, M. Analytical Seismic Fragility Analyses of Fire Sprinkler Piping Systems with Threaded Joints. *Earthq. Spectra* **2015**, *31*, 1125–1155. [CrossRef]
19. Soroushian, S.; Zaghi, A.E.; Maragakis, M. Seismic Fragility Study of Fire Sprinkler Piping Systems with Grooved Fit Joints. *J. Struct. Eng.* **2015**, *141*, 04014157. [CrossRef]
20. Rusnak, C.; Rivas, A.; Elfass, S. Experimental and Fragility Analysis of Threaded Cast Iron Pipe Fittings Utilized in a Fire Suppression System. *Front. Built Environ.* **2025**, *11*, 1565894. [CrossRef]
21. Rusnak, C.; Rivas, A.; Elfass, S. Comparison Between the Performance of Threaded Connections versus Welded Connections in Pipe-Fitting Assemblies. In Proceedings of the ASME 2024 Pressure Vessels and Piping Conference, Bellevue, WA, USA, 28 July–2 August 2024. PVP2024-123494.
22. Yoshizaki, K.; Hamada, A.; O'Rourke, T.D. Large Deformation Behavior of Buried Pipelines with Low-Angle Elbows Subjected to Permanent Ground Deformation. *J. Struct. Mech. Earthq. Eng. JSCE* **2001**, *18*, 41s–52s.
23. Engineers Edge. Material Strength—Strength (Mechanics) of Materials. Available online: https://www.engineersedge.com (accessed on 1 August 2025).
24. Hou, Y.; Mi, X.; Xie, H.; Zhang, W.; Huang, G.; Peng, L.P.; Feng, X.; Yang, Z. Size Effect on Mechanical Properties and Deformation Behavior of Pure Copper Wires Considering Free Surface Grains. *Materials* **2020**, *13*, 4563. [CrossRef] [PubMed]
25. Chen, H.; Yi, W.; Ma, Z.J. Shear Size Effect in Simply Supported RC Deep Beams. *Eng. Struct.* **2019**, *182*, 203–213. [CrossRef]
26. Bai, X.; Zhang, P.; Liu, S.; Zhao, B.; Zhang, Z. Fatigue Strength Prediction of Large-Size Component Through Size Effect Measurement and Determination. *Int. J. Fatigue* **2023**, *168*, 107281.
27. Gibson, D.; Forbes, I. Fire Suppression in Historic Buildings. Cathedral Communications Limited, 2019. Available online: https://www.buildingconservation.com/articles/firesup/fire_suppression.htm (accessed on 1 August 2025).
28. Archtoolbox. Standard Pipe Dimensions. Available online: https://www.archtoolbox.com/materials-systems/plumbing/standard-pipe-dimensions.html (accessed on 1 August 2025).
29. NFSA. *Technical Justifications for Large Diameter Fire Department Connections*; National Fire Sprinkler Association: Linthicum, MD, USA, 2020; Available online: https://nfsa.org/2020/05/01/technical-justification-for-large-diameter-fire-department-connections/ (accessed on 1 August 2025).
30. NFPA. *Automatic Sprinkler Systems Handbook, NFPA 13*; National Fire Protection Association: Quincy, MA, USA, 2022.

31. Chapman Electric Supply, Inc. Formulas for Calculation Conduit & Pipe Bends. Available online: https://www.chapmanelectric.com (accessed on 1 August 2025).
32. WSSC Water. *Water Design Guidelines. Part One, Section 13. Rotation of Fittings*; WSSC Water: Laurel, MD, USA, 2019.
33. ASME. *B16.4-2016: Gray Iron Threaded Fittings, Classes 125 and 250*; The American Society of Mechanical Engineers: New York, NY, USA, 2016.
34. ASC Engineered Solutions. *Anvil Cast Iron Threaded Fittings*; PS-SUB-351-v01; ASC Engineered Solutions: Navi Mumbai, India, 2021.
35. ASC Engineered Solutions. *Anvil Cast Iron Threaded Fittings*; PS-SUB-358-360-v01; ASC Engineered Solutions: Navi Mumbai, India, 2021.
36. ASME. *B1.20.1-2013: Pipe Threads, General Purpose (Inch)*; The American Society of Mechanical Engineers: New York, NY, USA, 2013.
37. ASME. *B31.3-2018: Process Piping, ASME Code for Pressure Piping*; The American Society of Mechanical Engineers: New York, NY, USA, 2018.
38. FEMA. *FEMA 461: Interim Testing Protocol for Determining the Seismic Performance Characteristics of Structural and Nonstructural Components*; Federal Emergency Management Agency: Washington, DC, USA, 2017.
39. Rusnak, C.; Elfass, A.; Rivas, A. Total Rotational Capacity of Threaded Connections in Pipe-Fitting Assemblies. In Proceedings of the ASME Pressure Vessels and Piping Conference 2024, Bellevue, WA, USA, 28 July–2 August 2024. PVP2024-123390.
40. FEMA. *P-58: Seismic Performance Assessment of Buildings*; Federal Emergency Management Agency: Washington, DC, USA, 2018.
41. Porter, K.; Kennedy, R.; Bachman, R. Creating Fragility Functions for Performance-Based Earthquake Engineering. *Earthq. Spectra* **2007**, *23*, 471–489. [CrossRef]
42. ASCE. *ASCE 7-22: Minimum Design Loads for Buildings and Other Structures*; American Society of Civil Engineers: Reston, VA, USA, 2022.